TOPICAL COLLECTION: ADVANCED METAL ION BATTERIES

NiCr-Cl LDH/rGO Composite as Anode Material for Sodium-Ion Batteries

Yi Zhang[1] · Yaru Zhang[1] · Liqun Ma[1,2] · Meng Yang[1,2] · Xiangyu Zhao[1,2]

Abstract

Layered double hydroxides (LDHs) have attracted increasing attention as anode materials for sodium-ion batteries (SIBs) due to their high theoretical specific capacity and simple preparation method. However, LDHs used as anode materials for SIBs still suffer from sluggish diffusion kinetics and huge volume change during the charge and discharge process, resulting in poor cycling performance and rate capability. Therefore, we fabricated a Cl^--intercalated NiCr layered double hydroxide/reduced graphene oxide (NiCr-Cl LDH/rGO) composite as an anode material for SIBs. Compared with pure $NiCr-CO_3$ LDH and $NiCr-CO_3$ LDH/rGO electrodes, the NiCr-Cl LDH/rGO electrode exhibited excellent cycling performance and rate capability, with the highest specific capacity of 218 mAh g^{-1} at current density of 100 mA g^{-1} for 200 cycles and 219 mAh g^{-1} at current density of 2.0 A g^{-1}. The superior Na^+ ion storage performance is attributed to the large interlayer spacing and the good electrical conductivity and flexibility of rGO. This work could provide a new path for constructing LDH-based composites as anode materials for SIBs in the field of energy storage.

Keywords Layered double hydroxides · reduced graphene oxide · composite · anode materials · sodium-ion batteries

Introduction

In recent years, rechargeable sodium-ion batteries (SIBs) have been regarded as prospective candidates for lithium-ion batteries (LIBs) due to the low cost and high natural abundance of sodium resources.[1–6] Anode materials are one of the crucial components of SIBs, and enormous efforts have been made to develop suitable anode materials for SIBs, such as alloy-type (Sn, Sb, and Bi)[7–9] and conversion-type (metal oxides, metal sulfides, and metal phosphides)[10–12] materials. However, most of these materials possess critical issues in which sluggish diffusion kinetics and large volume

✉ Liqun Ma
  maliqun@njtech.edu.cn

✉ Meng Yang
  yangmengyy@njtech.edu.cn

✉ Xiangyu Zhao
  xiangyu.zhao@njtech.edu.cn

1 College of Materials Science and Engineering, Nanjing Tech University, Nanjing 211816, China

2 Jiangsu Collaborative Innovation Center for Advanced Inorganic Functional Composites, Nanjing Tech University, Nanjing 211816, China

change during the charge and discharge process can cause poor cycling performance and rate capability.[13,14] Therefore, the development of advanced anode materials for SIBs with highly reversible insertion and extraction of Na^+ ions is a huge challenge.

Layered double hydroxides (LDHs) are a type of two-dimensional (2D) brucite-like material composed of a bimetal octahedral layer host and interlayer anion guest, and their general formula is expressed by $M_x^{2+}M_y^{3+}(OH)_{2(x+y)} \cdot (A^{n-})_{y/n} \cdot mH_2O$ (M: metal, A^{n-}: interlayer anion).[15,16] Because of their high theoretical specific capacity and simple preparation method, LDHs have attracted extensive attention as anode materials for LIBs,[16–20] but are seldom applied as the anode materials for SIBs. To date, only $CoFe-NO_3$ LDH[21] has been reported as an anode material for SIBs and delivers a reversible capacity of 209 mAh g^{-1} over 200 cycles at 1000 mA g^{-1}. However, LDHs demonstrate low intrinsic electrical conductivity and huge volume change during the charge and discharge process,[22] which greatly affects the electrochemical performance of SIBs. Graphene materials with mechanical flexibility, good electrical conductivity, and large surface area are regarded as suitable substrate materials to enhance the electrochemical performance of LDHs,[17,19,23–25] which not only can improve the electronic conductivity of LDHs but also can relieve the huge

volume change of LDHs during cycling. Therefore, constructing LDH composites with graphene materials can remarkably improve the cycling performance and rate capability of LDHs.

Herein, NiCr-Cl LDH/rGO composites were successfully synthesized via a one-step hydrothermal method, followed by an ion exchange process. The morphology and structural characteristics were systematically studied, and the electrochemical properties of the as-prepared materials as anodes for SIBs were investigated. The as-prepared NiCr-Cl LDH/rGO composite displayed initial discharge capacity of 632 mAh g^{-1}, reversible capacity of 466.9 mAh g^{-1} after 200 cycles, and superior rate performance as compared with the NiCr-CO$_3$ LDH and NiCr-CO$_3$ LDH/rGO.

Experimental Section

NiCr-Cl LDH/rGO composite was obtained from NiCr-CO$_3$ LDH/rGO material by ion exchange, wherein NiCr-CO$_3$ LDH/rGO was synthesized by a one-step hydrothermal method. NiCl$_2$·6H$_2$O, CrCl$_3$·6H$_2$O, and NH$_4$F were dissolved in 60 mL GO dispersion (1.67 mg/mL), in which the total concentration of metal ions was 4 mmol and the ratio of Ni^{2+}/Cr^{3+} was 3:1. The concentration of NH$_4$F was twice that of the metal ion. A total of 7 mmol urea was added to the above system under vigorous stirring to form a homogeneous suspension. The suspension was transferred to a 100 mL Teflon-lined stainless-steel autoclave at 150°C for 24 h. The autoclave was then cooled to room temperature naturally. The sample was washed with deionized water and ethanol and dried in a vacuum freezing dryer to obtain the NiCr-CO$_3$ LDH/rGO composite. The obtained NiCr-CO$_3$ LDH/rGO composite was added to 500 mL of NaCl/HCl mixed solution and stirred for 24 h under an N$_2$ airtight atmosphere. The product was washed and dried to obtain the NiCr-Cl LDH/rGO composite. Graphene oxide (GO) was synthesized by the modified Hummers method.[26]

X-ray diffraction (XRD) data were recorded by an x-ray diffractometer using Cu-Kα ($\lambda = 0.15418$ nm) radiation (Rigaku, SmartLab) with a scanning rate of 10°/min in the range of 5–70°, operating at 40 kV and 40 mA. The morphology and microstructure of the samples were analyzed using field-emission scanning electron microscopy (FE-SEM, Zeiss Gemini Ultra 55) with an accelerating voltage of 20 kV and transmission electron microscopy (TEM, JEOL JEM-2100). X-ray photoelectron spectroscopy (XPS) measurements were carried out on an ESCALAB 250 spectrometer (Thermo Fisher) using a focused monochromatized Al Kα ($h\nu = 1486.6$ eV) as the excitation source. The binding energy of C 1s at 284.8 eV was taken as a reference for the calibration. Thermogravimetric analysis (TG) data were recorded using an STA 409PC (NETZSCH) in a nitrogen atmosphere at a heating rate of 10°C/min. N$_2$ adsorption/

desorption measurement data were recorded by a Quantachrome Autosorb-1 automatic volumetric instrument.

The electrochemical measurements of the materials were carried out at room temperature using coin cells. The NiCr-CO$_3$ LDH, NiCr-CO$_3$ LDH/rGO, and NiCr-Cl LDH/rGO electrodes were prepared by mixing 60 wt.% active material, 30 wt.% acetylene black, and 10 wt.% PVDF, which were dissolved in NMP to form a homogeneous slurry. The obtained slurry was cast on a copper foil and dried for 12 h at 80°C under a vacuum. The as-prepared electrode and sodium foil were used as the working and counter electrodes, respectively. Glass fiber (Whatman) was chosen as a separator, and 1 M NaCF$_3$SO$_3$ dissolved in diglyme was used as the electrolyte. Galvanostatic charge and discharge test was carried out using a Neware battery system in a voltage range of 0.3–3 V versus Na$^+$/Na at room temperature. Cyclic voltammograms (CV) data were obtained using a VMP3 potentiostat/galvanostat (BioLogic Science Instruments) at a scan rate of 0.1 mV s^{-1} between 0.3 and 3.0 V (vs. Na$^+$/Na). Electrochemical impedance spectra (EIS) were also measured on a VMP3 potentiostat/galvanostat with a range of 10^5 to 0.01 Hz.

Results and Discussion

Figure 1a shows the powder XRD patterns of the as-prepared NiCr-CO$_3$ LDH (denoted as NCC), NiCr-CO$_3$ LDH/rGO (denoted as NCC/rGO), and NiCr-Cl LDH/rGO samples (denoted as NCCl/rGO). All the diffraction peaks of the three samples can be assigned to the layered hydrotalcite-like structure (PDF: 52-1626) with the *R-3m* space group.[27,28] However, a huge discrepancy in the intensity of the diffraction peaks for the samples with/without rGO was observed, indicating that the introduced rGO can suppress grain growth. In addition, after chloride ion exchange, the (003) diffraction peak position of LDH moves from 11.6° to 11.3°, indicating an increased d-spacing. Figure 1b shows the Fourier transform–infrared (FT-IR) spectra of as-prepared NCC, NCC/rGO, and NCCl/rGO. Absorption peaks below 800 cm^{-1} are associated with M–O/M–OH (M=Ni, Cr) stretching and bending vibrations in the LDH laminate.[28,29] Absorption peaks located at 1640 cm^{-1} are assigned to the O–H stretching vibrations caused by interlayer crystal water.[30] The peak at 1358 cm^{-1} corresponds to the asymmetric stretching vibration of CO$_3^{2-}$, denoted as V$_3$(CO$_3^{2-}$). However, an evident discrepancy is observed when comparing the FT-IR spectra of NCC and NCC/rGO, and this can be reflected by the new peaks at 1399 and 1214 cm^{-1}. The peak located at 1399 cm^{-1} corresponds to the C–OH stretching vibrations of rGO, while the peak located at 1214 cm^{-1} may be caused by the interaction between LDH and rGO. After chloride
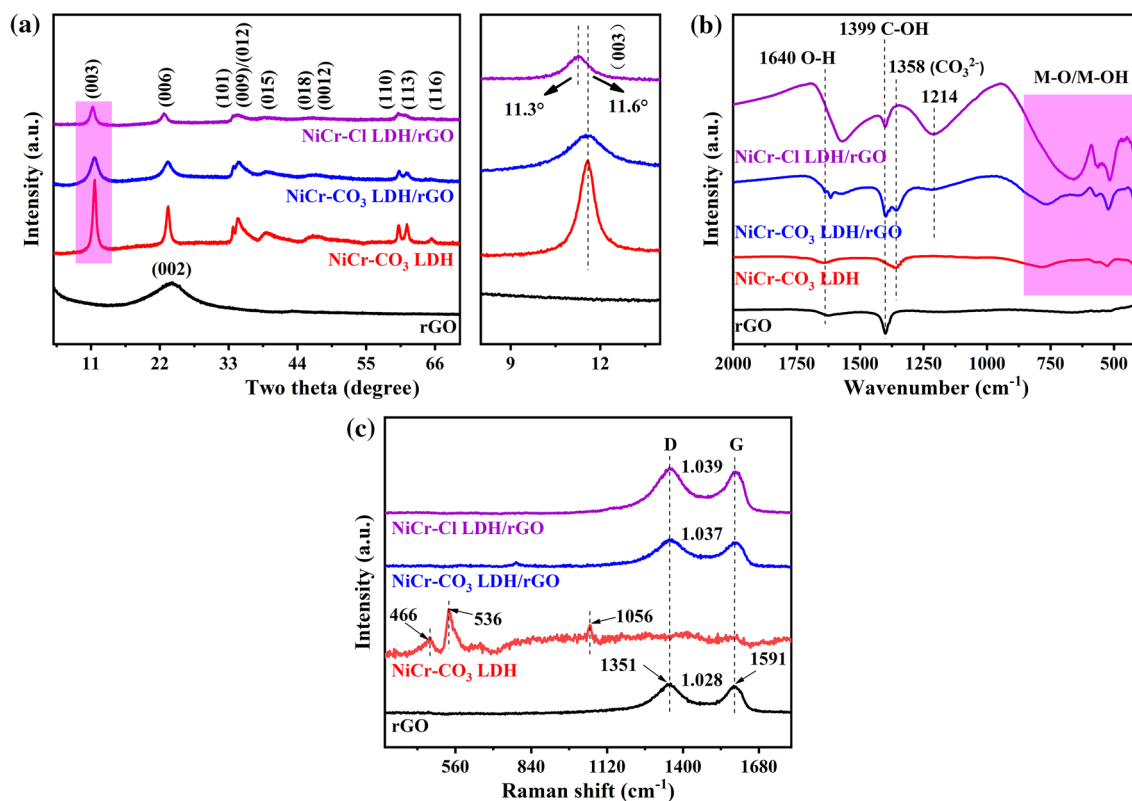
Fig. 1 XRD patterns (a), FT-IR spectra (b), and Raman spectra, (c) of NCC, NCC/rGO, and NCCl/rGO.

ion exchange, the characteristic peak of $V_3(CO_3^{2-})$ in the LDH interlayer disappears, which suggests that the CO_3^{2-} ions were successfully replaced by Cl^- ions.[31,32] In addition, the intensity of the absorption peaks located at 1214 cm^{-1} increases, ascribed to the enhanced interaction between LDH and rGO. Figure 1c shows the Raman spectra of as-prepared NCC, NCC/rGO, and NCCl/rGO. For the NCC sample, three characteristic Raman peaks at 466 cm^{-1}, 536 cm^{-1} and 1056 cm^{-1} can be observed. The peaks at 466 cm^{-1} and 536 cm^{-1} are associated with the A_{1g} Raman-active vibrational modes of $Ni(OH)_2$ and $Cr(OH)_3$, respectively. The peak at 1056 cm^{-1} is ascribed to the symmetric stretching vibration of CO_3^{2-} ions in the LDH interlayer.[29] In the case of NCC/rGO and NCCl/rGO, two bands from rGO (D band at 1351 cm^{-1}, G band at 1591 cm^{-1}) can be observed, suggesting the successful synthesis of the LDH/rGO composite.[33] Moreover, the NCC/rGO and NCCl/rGO samples demonstrate higher relative intensity of the D band than that of rGO, which is due to the formation of chemical bonds between rGO and LDH, leading to the formation of more defects.[17] The TG results (see supplementary Fig. S1) indicate that the graphene content of the NCC/rGO composite is 6.01 wt.%.[17]

Figure 2 shows the SEM and TEM images of as-prepared NCC, NCC/rGO, and NCCl/rGO. As illustrated in Fig. 2a,

b, and c, the as-prepared NCC exhibits a flower-like sphere with an interconnected nanosheet structure. Figure 2d, e, and f suggests that LDH nanosheets with thickness of about 20 nm are uniformly grown on the rGO sheets' surfaces, which can be further confirmed by EDS mapping images (see supplementary Fig. S2a). However, the morphology of NCCl/rGO exhibits an evident change where the rGO sheets give rise to an apparent agglomeration phenomenon (Fig. 2g, h, i, and j), which may be due to the enhanced interaction between LDH and rGO after the ion exchange. The uniform distribution of Ni, Cr, and Cl elements (see supplementary Fig. S2) indicates uniform intercalation of Cl^- ions in the LDH interlayer. The calculated ratio of Ni/Cr/Cl is close to 3:1:1 (see supplementary Fig. S3).

The surface composition and valence states of the as-prepared NCCl/rGO are measured by XPS, as presented in Fig. 3. It can be found from the width spectrum that the NCCl/rGO mainly consists of Ni, Cr, C, O, and Cl elements (Fig. 3a). For the XPS high-resolution C 1s spectrum (Fig. 3b), it can be divided into four peaks, corresponding to different carbon-containing functional groups, including C=C/C–C bonds (284.82 eV), C-O bonds (285.77 eV), the C=O bonds (286.72 eV) and C(O)O bonds (289.03 eV. The Ni 2p spectrum (Fig. 3c) includes two main peaks of Ni $2p_{3/2}$ (856.20 eV) and Ni $2p_{1/2}$ (873.71 eV) peaks accompanied
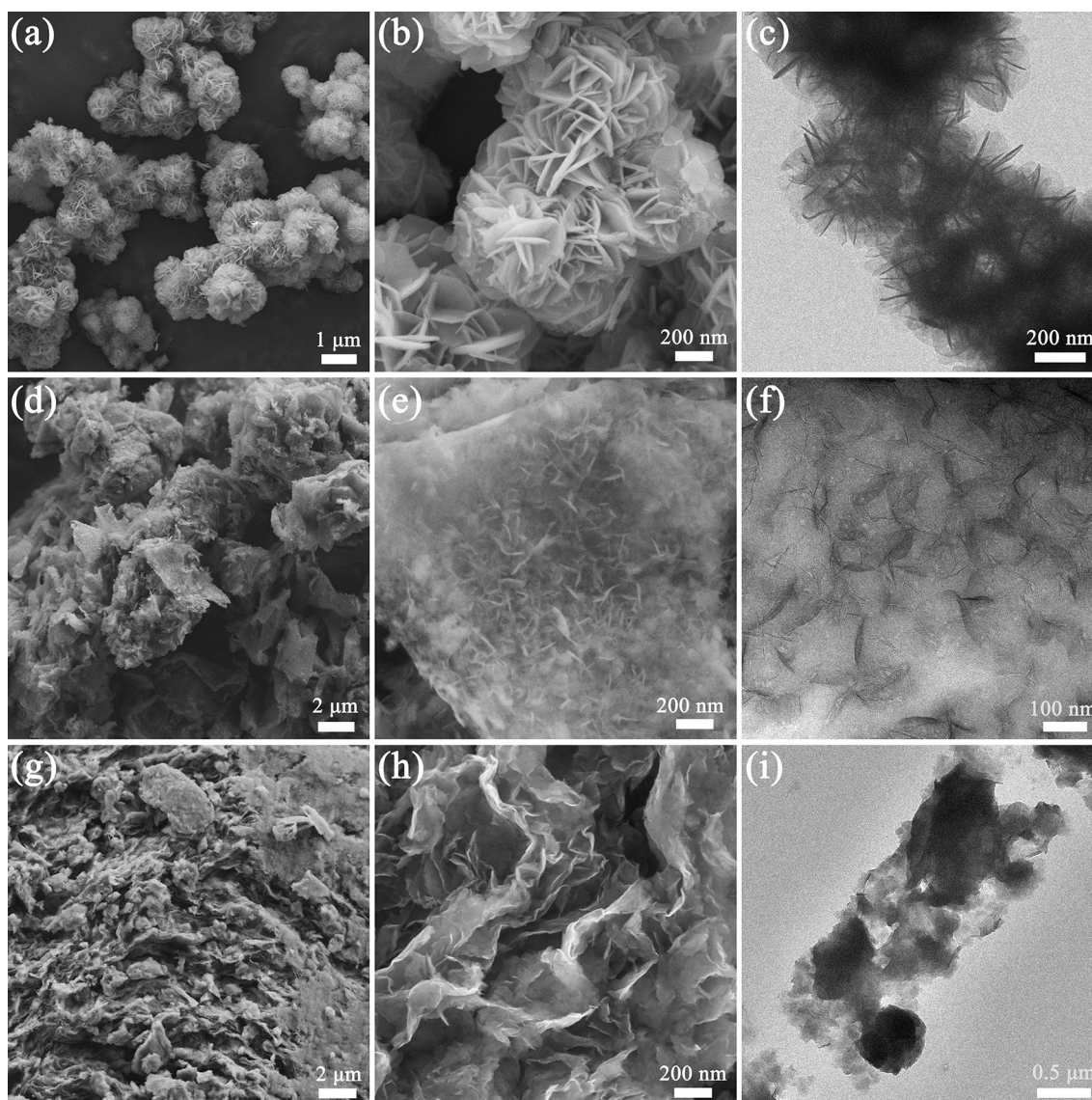
Fig. 2 SEM and TEM images of NCC (a–c), NCC/rGO (d–f), and NCCl/rGO (g–i).

by two satellite peaks at 862.03 eV and 879.73 eV, which confirm the existence of the Ni^{2+} state.[29,34,35] Besides, the Cr 2*p* characteristic peaks at binding energy of 577.48 eV and 587.3 eV correspond to the spin–orbit doublet of Cr $2p_{3/2}$ and Cr $2p_{1/2}$ (Fig. 3d), respectively. This result demonstrates the presence of the Cr^{3+} state.[29,36] The XPS signals of Cr $2p_{3/2}$ are divided into two peaks located at binding energy of 577.48 eV and 579.18 eV, which can be attributed to the formation of Cr–OH and Cr–O bonds in the LDH, respectively.[37]

The N_2 adsorption/desorption measurements were carried out to study the porous structure of NCC, NCC/rGO, and NCCl/rGO. Figure 4 shows the isotherms and the corresponding pore size distribution curves. The isotherms of NCC and NCC/rGO reveal an H3-type hysteresis loop,

while the isotherm of NCCl/rGO reveals an H2-type hysteresis loop, indicating the presence of a mesoporous structure for the three samples.[38] Table S1 (see supplementary data file) shows that the pore distribution range of NCC/rGO (2–120 nm) is bigger than that of NCC and NCCl/rGO. Moreover, the specific surface area of NCC/rGO (170.44 m² g⁻¹) is larger than that of the NCC, owing to the uniform growth of LDH nanosheets on rGO sheets to form a three-dimensional (3D) network structure.[39] Possessing a larger specific surface area and unique porous structure, the NCC/rGO can provide more reaction active sites.

The electrochemical properties of as-prepared NCC, NCC/rGO, and NCCl/rGO electrodes are shown in Fig. 5. Figure 5a, b, and c show that these three electrodes exhibit evident irreversible reactions near 0.5 V in the
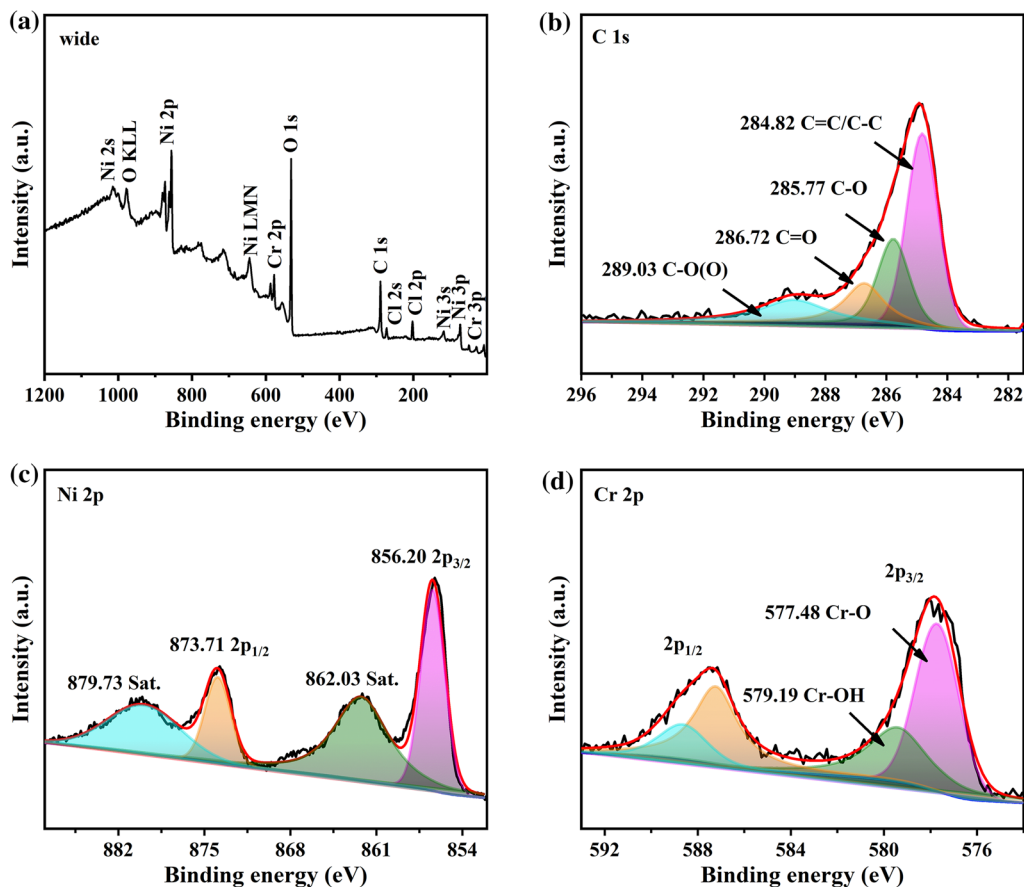
Fig. 3 The XPS wide spectra (a) and high-magnification spectra (b) C 1*s*, (c) Ni 2*p*, and (d) Cr 2*p* of NCCl/rGO.
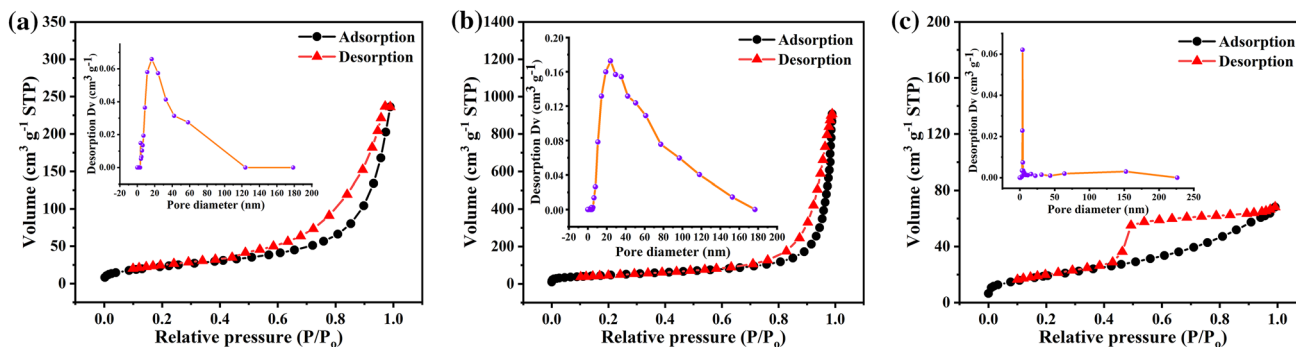
Fig. 4 Nitrogen adsorption–desorption isotherms and their corresponding pore size distribution of the as-prepared NCC (a), NCC/rGO (b), and NCCl/rGO (c).

first reduction, corresponding to the formation of a solid electrolyte interface (SEI) film on the electrode surface by electrolyte decomposition.[40,41] The corresponding oxidation process is reflected by three weak oxidation peaks located at 1.10 V, 1.63 V, and 2.02 V in the reverse scan, respectively. In the subsequent cycles, the CV curves display a broad reduction region at 0.5 V, which corresponds to the

reversible reduction reactions of Ni and Cr. However, upon further cycling, all three electrodes show a decreased peak current in various degrees. The galvanostatic charge and discharge results indicate that all three electrodes present similar charge and discharge profiles, as shown in Fig. 5d, e, and f. During the first cycle, a distinguishable discharge voltage plateau appears at about 0.5 V, but the corresponding charge
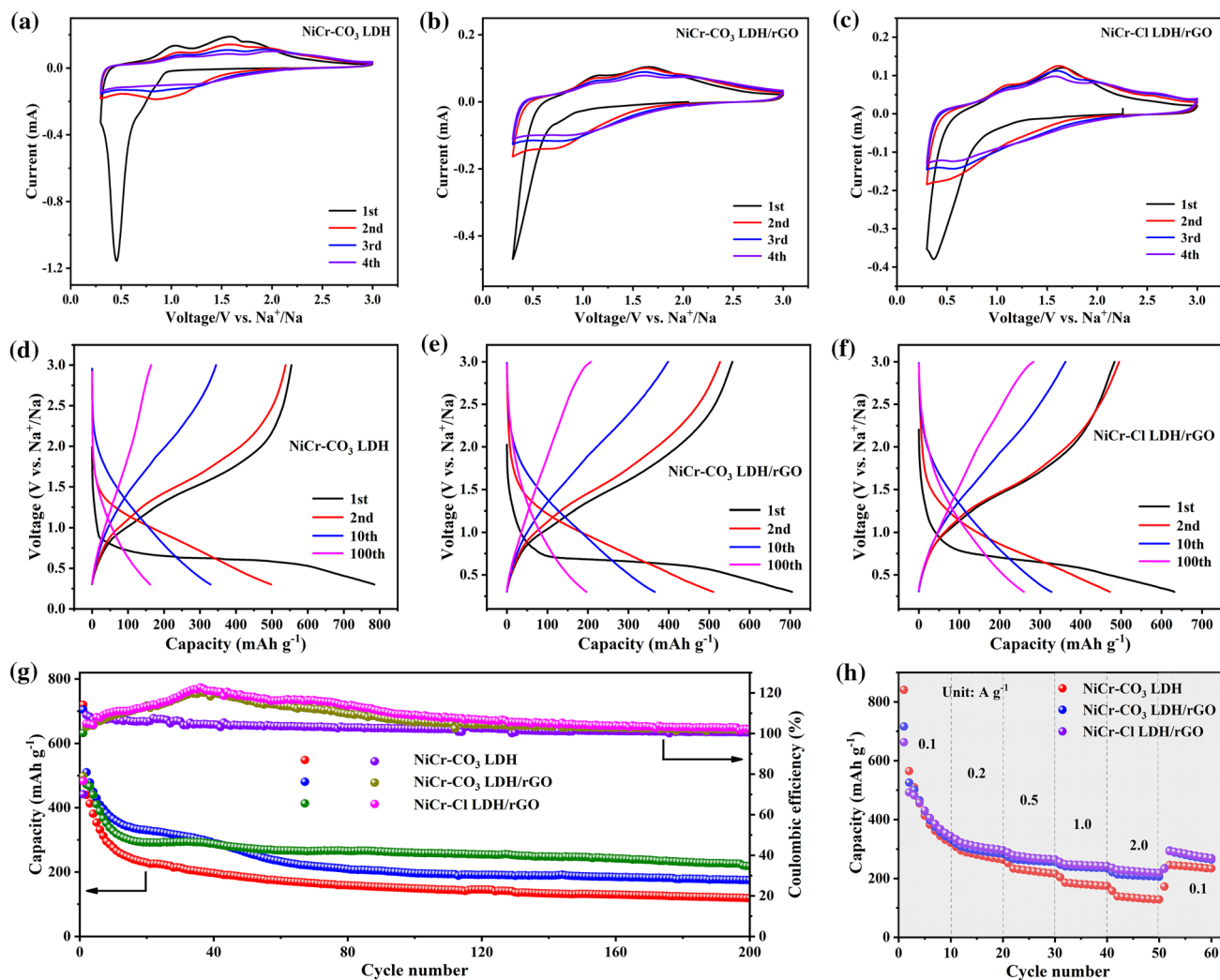
Fig. 5 CV and galvanostatic charge–discharge curves of NCC (a, d), NCC/rGO (b, e), and NCCl/rGO (c, f) electrodes. Cycling performance and coulombic efficiency (g) in 200 cycles at 100 mA g^{-1}. Rate capability (h) of the as-prepared NCC, NCC/rGO, and NCCl/rGO electrodes.

curves show three voltage regions with different slopes. In the subsequent cycles, the discharge curves show an obvious difference, and the discharge voltage plateau at 0.5 V has disappeared. In spite of a large irreversible capacity in the first cycle, these three electrodes still deliver a discharge capacity close to 500 mAh g^{-1} in the second cycle. Figure 5g shows the long cycling performance coulombic efficiency of the NCC, NCC/rGO, and NCCl/rGO electrodes. The coulombic efficiency is calculated based on the ratio of charge capacity to discharge capacity. All the electrodes suffer considerable capacity decay within the initial 15 cycles. However, comparing the three electrodes, it can be found that the NCCl/rGO electrode delivers relatively good cycling stability. After 200 cycles, the discharge capacity decreases from 632 mAh g^{-1} to 218 mAh g^{-1}, corresponding to a capacity retention of 34.5%. In contrast, the NCC electrode delivers capacity retention of only about 16.5%

after 200 cycles. The rGO electrode exhibits stable capacity of about 90.0 mAh g^{-1} (see supplementary Fig. S4). The capacity (5.4 mAh g^{-1}) contribution by the 6.0 wt.% rGO in the NCC/rGO electrode is negligible. The rate capability test of these three electrodes was performed at various current density values, as shown in Fig. 5h. The NCCl/rGO electrode has better rate capability than the other two electrodes, and delivers discharge capacities of 343 mAh g^{-1}, 296 mAh g^{-1}, 265 mAh g^{-1}, 242 mAh g^{-1}, and 219 mAh g^{-1} at current density of 0.1 A g^{-1}, 0.2 A g^{-1}, 0.5 A g^{-1}, 1 A g^{-1}, and 2 A g^{-1}, respectively. The superior cycling performance and rate capability of the NCCl/rGO electrode benefit from the existence of rGO and the large interlayer spacing of LDH. Figure S5 (see supplementary data file) shows the electrochemical impedance spectroscopy (EIS) measurements of the three electrodes. Generally, the semicircles at high frequency represent the charge transfer resistance (Rct),

and the slope at low frequency represents capacitive behavior and ion diffusion resistance.[25,42] It is observed that the three electrodes have apparent semicircles and slope. The Rct value (see supplementary Table S2) of the NCCl/rGO electrode is the smallest of these three electrodes, implying that the rGO improves the electrical conductivity of LDH, which enhances the electrochemical performance of LDH.

The kinetic behavior of the NCCl/rGO electrode was investigated by CV measurements. Figure 6a displays the CV curves at different scan rates from 0.2 mV s^{-1} to 1.0 mV s^{-1}. With the increase in the scan rates, the profiles of CV curves are nearly unchanged and the peak current increases gradually. The log(i) versus log(v) profiles are shown in Fig. 6b according to the functional relationship of peak current (i) and scan rate (v) ($i = av^b$) (i value was obtained by measuring, a is an adjustable parameter, b is the slope of a profile of log(i) versus log (v), $b = 0.5$ represents the diffusion-controlled process while $b = 1$ suggests a capacitive process, the ratio of capacitive contribution is determined by the equation $i = k_1 v + k_2 v^{1/2}$, the $k_1 v$ and $k_2 v^{1/2}$ represent the capacitive behavior and diffusion effects, respectively).[43] The b valve (0.78 and 0.91) is between 0.5 and 1 and closer to 1, which indicates that the Na$^+$ ion storage kinetics are simultaneously controlled by capacitive and diffusion processes while the former dominates. Figure 6c and d show that the NCCl/rGO electrode has a capacitive contribution ratio of 55.1% at 0.2 mV s^{-1}, which confirms the capacitive-controlled kinetic behavior. The high capacitive contribution results in excellent Na$^+$ ion storage performance of LDH with a long cycle life and high rate capability.

Conclusions

In summary, we synthesized NiCr-Cl LDH/rGO composite by hydrothermal and ion exchange methods. The NiCr-Cl LDH/rGO electrode exhibits excellent cycling performance and rate capability, with the highest specific capacity of 218 mAh g^{-1} at current density of 100 mA g^{-1} for 200 cycles and 219 mAh g^{-1} at current density of 2.0 A g^{-1}. The excellent Na$^+$ ion storage electrochemical performance is attributed to the expanded interlayer spacing of LDH, the good electrical conductivity of rGO, and the flexibility of rGO. The expanded interlayer spacing of LDH can provide enough channels to accommodate the migration of Na$^+$ ions. Besides, the flexible rGO not only endows the NiCr-Cl LDH/
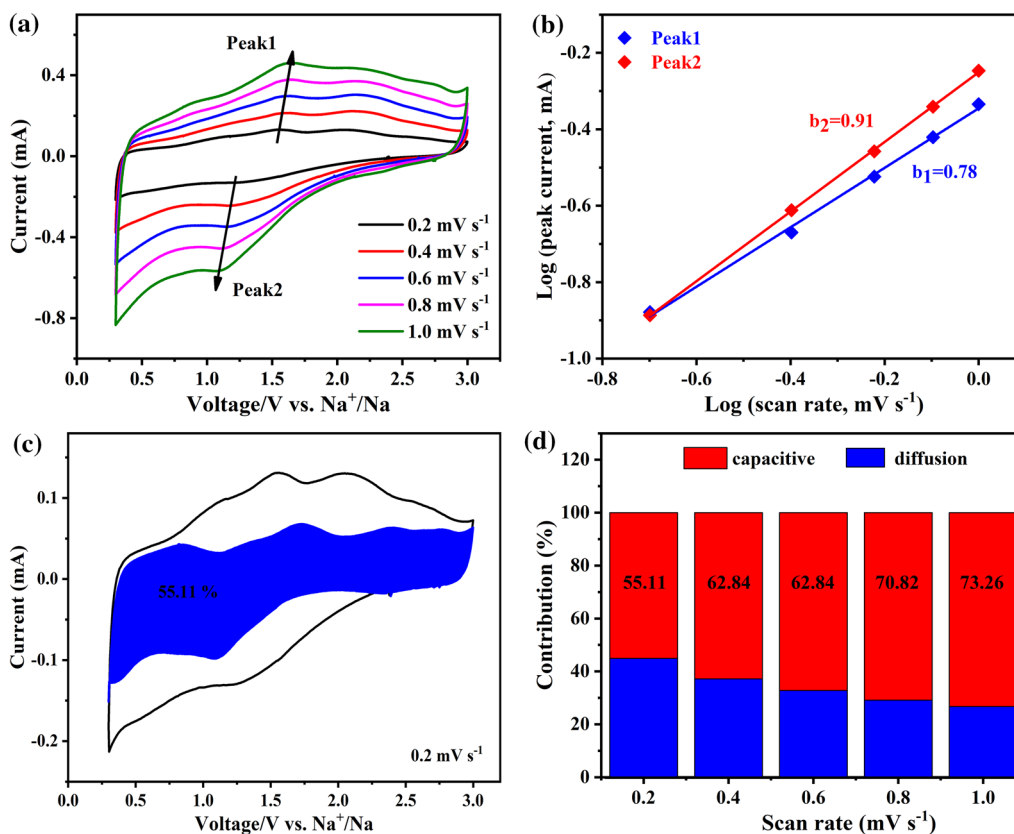
Fig. 6 Kinetics analysis of the as-prepared NCCl/rGO electrode. (a) CV curves at different scan rates. (b) Log(i) versus log(v) profiles. (c) CV curves with the capacitive contribution at 0.2 mV s^{-1}. (d) The ratio histogram of capacitance and diffusion-controlled capacities.

rGO composite with good electrical conductivity but also provides a good buffer zone to relieve the volume change of LDH during the charge and discharge process. This work provides a new path for using LDH-based composites as anode materials for SIBs, which is concerned with the application of LDH-based composites in the field of energy storage.

References

1. M. Slater, D. Kim, E. Lee, and C. Johnson, Sodium-Ion Batteries. *Adv. Funct. Mater.* 23, 947 (2013).
2. Y. Kim, K. Ha, S. Oh, and K. Lee, High-Capacity Anode Materials for Sodium-Ion Batteries. *Chem* 20, 11980 (2014).
3. J. Hwang, S. Myung, and Y. Sun, Sodium-Ion Batteries: Present and Future. *Chem. Soc. Rev.* 46, 3529 (2017).
4. X. Yuan, S. Chen, J. Li, J. Xie, G. Yan, B. Liu, X. Li, R. Li, L. Pan, and W. Mai, Understanding the Improved Performance of Sulfur-Doped Interconnected Carbon Microspheres for Na-Ion Storage. *Carbon Energy* 3, 615 (2021).
5. L. Zhang, C. Wei, X. Fu, Z. Chen, B. Yan, P. Sun, K. Chang, and X. Yang, Ternary Ni-Based Prussian Blue Analogue with Superior Sodium Storage Performance Induced by Synergistic Effect of Co and Fe. *Carbon Energy* 3, 827 (2021).
6. C. Wang, Y. Li, F. Cao, Y. Zhang, X. Xia, and L. Zhang, Employing Ni-Embedded Porous Graphitic Carbon Fibers for High-Efficiency Lithium-Sulfur Batteries. *ACS Appl. Mater. Interfaces* 14, 10457 (2022).
7. N. Yabuuchi, K. Kubota, M. Dahbi, and S. Komaba, Research Development on Sodium-Ion Batteries. *Chem. Rev.* 114, 11636 (2014).
8. S. Liang, Y. Cheng, J. Zhu, Y. Xia, and P. Müller-Buschbaum, A Chronicle Review of Nonsilicon (Sn, Sb, Ge)-Based Lithium/Sodium-Ion Battery Alloying Anodes. *Small Methods* 4, 2000218 (2020).
9. M. Wang, F. Zhang, C. Lee, and Y. Tang, Low-Cost Metallic Anode Materials for High Performance Rechargeable Batteries. *Adv. Energy Mater.* 7, 1700536 (2017).
10. Y. He, P. Xu, B. Zhang, Y. Du, B. Song, X. Han, and H. Peng, Ultrasmall MnO Nanoparticles Supported on Nitrogen-Doped Carbon Nanotubes as Efficient Anode Materials for Sodium Ion Batteries. *ACS Appl. Mater. Interfaces* 9, 38401 (2017).
11. Y. Kim, Y. Kim, A. Choi, S. Woo, D. Mok, N. Choi, Y. Jung, J. Ryu, S. Oh, and K. Lee, Tin Phosphide as a Promising Anode Material for Na-Ion Batteries. *Adv. Mater.* 26, 4139 (2014).
12. D. Sun, D. Ye, P. Liu, Y. Tang, J. Guo, L. Wang, and H. Wang, MoS$_2$/Graphene Nanosheets from Commercial Bulky MoS$_2$ and Graphite as Anode Materials for High Rate Sodium-Ion Batteries. *Adv. Energy Mater.* 8, 1702383 (2018).
13. Y. Fang, L. Xiao, X. Ai, Y. Cao, and H. Yang, Hierarchical Carbon Framework Wrapped Na$_3$(PO$_4$)$_3$ as a Superior High-Rate and Extended Lifespan Cathode for Sodium-Ion Batteries. *Adv. Mater.* 27, 5895 (2015).
14. T. Zhu, P. Hu, X. Wang, Z. Liu, W. Luo, K. Owusu, W. Cao, C. Shi, J. Li, L. Zhou, and L. Mai, Realizing Three-Electron Redox Reactions in NASICON-Structured Na$_3$MnTi(PO$_4$)$_3$ for Sodium-Ion Batteries. *Adv. Energy Mater.* 9, 1803436 (2019).
15. J. Yu, Q. Wang, D. O'Hare, and L. Sun, Preparation of Two Dimensional Layered Double Hydroxide Nanosheets and Their Applications. *Chem. Soc. Rev.* 46, 5950 (2017).
16. Q. Wang, and D. O'Hare, Recent Advances in the Synthesis and Application of Layered Double Hydroxide (LDH) Nanosheets. *Chem. Rev.* 112, 4124 (2012).
17. M. Tian, C. Liu, Z.G. Neale, J. Zheng, D. Long, and G. Cao, Chemically Bonding NiFe-LDH Nanosheets on rGO for Superior Lithium-Ion Capacitors. *ACS Appl. Mater. Interfaces* 11, 35977 (2019).
18. C. Li, D. Zhang, J. Cao, P. Yu, M. Okhawilai, J. Yi, J. Qin, and X. Zhang, Ti$_3$C$_2$ Mxene-Encapsulated NiFe-LDH Hybrid Anode for High-Performance Lithium-Ion Batteries and Capacitors. *ACS Appl. Energy Mater.* 4, 7821 (2021).
19. L. Shi, Y. Chen, R. He, X. Chen, and H. Song, Graphene-Wrapped CoNi-Layered Double Hydroxide Microspheres as a New Anode Material for Lithium-Ion Batteries. *Phys. Chem. Chem. Phys.* 20, 16437 (2018).
20. S. Karthik Kiran, S. Shukla, A. Struck, and S. Saxena, Surface Engineering of Graphene Oxide Shells Using Lamellar LDH Nanostructures. *ACS Appl. Mater. Interfaces* 11, 20232 (2019).
21. Y. Zhao, T. Sun, Q. Yin, J. Zhang, S. Zhang, J. Luo, H. Yan, L. Zheng, J. Han, and M. Wei, Discovery of a New Intercalation-Type Anode for High-Performance Sodium Ion Batteries. *J. Mater. Chem. A* 7, 15371 (2019).
22. R. Zhang, Z. Xue, J. Qin, M. Sawangphruk, X. Zhang, and R. Liu, NiCo-LDH/Ti$_3$C$_2$ MXene Hybrid Materials for Lithium Ion Battery with High-Rate Capability and Long Cycle Life. *J. Energy Chem.* 50, 143 (2020).
23. S. Yang, Z. Zhang, J. Zhou, Z. Sui, and X. Zhou, Hierarchical NiCo LDH-rGO/Ni Foam Composite as Electrode Material for High-Performance Supercapacitors. *Trans. Tianjin Univ.* 25, 266 (2018).
24. S. Kiran, S. Shukla, A. Struck, and S. Saxena, Surface Enhanced 3D rGO Hybrids and Porous rGO Nano-networks as High Performance Supercapacitor Electrodes for Integrated Energy Storage Devices. *Carbon* 158, 527 (2019).
25. F. Song, R. Zhang, X. Zhang, J. Qin, and R. Liu, Ni-Co Double Hydroxide Grown on Graphene Oxide for Enhancing Lithium Ion Storage. *Energy Fuels* 34, 13032 (2020).
26. M.J. Yoo, and H.B. Park, Effect of Hydrogen Peroxide on Properties of Graphene Oxide in Hummers Method. *Carbon* 141, 515 (2019).
27. S. Gamil, M. Antuch, I.T. Zedan, and W.M.A. El Rouby, 3D NiCr-Layered Double Hydroxide/Reduced Graphene Oxide Sand Rose-Like Structure as Bifunctional Electrocatalyst for Methanol Oxidation. *Colloids Surf. A* 602, 125067 (2020).
28. F.M. Labajos, and V. Rives, Thermal Evolution of Chromium(III) Ions in Hydrotalcite-Like Compounds. *Inorg. Chem.* 33, 5313 (1996).
29. N. Padalkar, S. Sadavar, R. Shinde, A. Patil, U. Patil, D. Dhawale, H. Pathan, S. Sartale, V. Parale, A. Vinu, C. Lokhande, and J. Gunjakar, Mesoporous Nanohybrids of 2D Ni-Cr-Layered Double Hydroxide Nanosheets Pillared with Polyoxovanadate Anions for High-Performance Hybrid Supercapacitor. *Adv. Mater. Interfaces* 9, 2101216 (2021).

30. M. Li, F. Liu, X.B. Zhang, and J.P. Cheng, A Comparative Study of Ni-Mn Layered Double Hydroxide/Carbon Composites with Different Morphologies for Supercapacitors. *Phys. Chem. Chem. Phys.* 18, 30068 (2016).

31. Q. Yin, J. Luo, J. Zhang, L. Zheng, G. Cui, J. Han, and D. O'Hare, High-Performance, Long Lifetime Chloride Ion Battery Using a NiFe-Cl Layered Double Hydroxide Cathode. *J. Mater. Chem. A* 8, 12548 (2020).

32. Q. Yin, J. Luo, J. Zhang, S. Zhang, J. Han, Y. Lin, J. Zhou, L. Zheng, and M. Wei, Ultralong-Life Chloride Ion Batteries Achieved by the Synergistic Contribution of Intralayer Metals in Layered Double Hydroxides. *Adv. Funct. Mater.* 30, 1907448 (2019).

33. Z. Gao, J. Liang, J. Yao, Y. Zhao, Q. Meng, G. He, and H. Chen, Synthesis of Ce-Doped NiAl LDH/RGO Composite as an Efficient Photocatalyst for Photocatalytic Degradation of Ciprofloxacin. *J. Environ. Chem. Eng.* 9, 105405 (2021).

34. J. Luo, Q. Yin, J. Zhang, S. Zhang, L. Zheng, and J. Han, NiMn-Cl Layered Double Hydroxide/Carbon Nanotube Networks for High-Performance Chloride Ion Batteries. *ACS Appl. Energy Mater.* 3, 4559 (2020).

35. G. Jia, Y. Hu, Q. Qian, Y. Yao, S. Zhang, Z. Li, and Z. Zou, Formation of Hierarchical Structure Composed of (Co/Ni)Mn-LDH Nanosheets on MWCNT Backbones for Efficient Electrocatalytic Water Oxidation. *ACS Appl. Mater. Interfaces* 8, 14527 (2016).

36. X. Zhang, X. Sun, Y. Li, F. Hu, Y. Xu, J. Tian, H. Zhang, Q. Liu, H. Su, and S. Wei, Reduced Interfacial Tension on Ultrathin NiCr-LDH Nanosheet Arrays for Efficient Electrocatalytic Water Oxidation. *J. Mater. Chem. A* 9, 16706 (2021).

37. W. Ye, X. Fang, X. Chen, and D. Yan, A Three-Dimensional Nickel-Chromium Layered Double Hydroxide Micro/nanosheet Array as an Efficient and Stable Bifunctional Electrocatalyst for Overall Water Splitting. *Nanoscale* 10, 19484 (2018).

38. W. Zhang, C. Ma, J. Fang, J. Cheng, X. Zhang, S. Dong, and L. Zhang, Asymmetric Electrochemical Capacitors with High Energy and Power Density Based on Graphene/CoAl-LDH and Activated Carbon Electrodes. *RSC Adv.* 3, 2483 (2013).

39. J. Liang, Y. Wei, Y. Yao, X. Zheng, J. Shen, G. He, and H. Chen, Constructing High-Efficiency Photocatalyst for Degrading Ciprofloxacin: Three-Dimensional Visible Light Driven Graphene Based NiAlFe LDH. *J. Colloid Interface Sci.* 540, 237 (2019).

40. Q. Lin, J. Zhang, D. Kong, T. Cao, S.-W. Zhang, X. Chen, Y. Tao, W. Lv, F. Kang, and Q.-H. Yang, Deactivating Defects in Graphenes with Al_2O_3 Nanoclusters to Produce Long-Life and High-Rate Sodium-Ion Batteries. *Adv. Energy Mater.* 9, 1803078 (2019).

41. J. Zhou, S. Cheng, Y. Jiang, F. Zheng, L. Yang, H. Rong, X. Ou, P. Wu, Y. Zhu, and M. Liu, High Rate and High Capacity Lithiation of rGO-Coated $Co_2(OH)_2CO_3$ Nanosheet Arrays for Lithium-Ion Batteries Through the Involvement of CO_3^{2-}. *Electrochim. Acta* 235, 98 (2017).

42. W. Peng, H. Li, and S. Song, Synthesis of Fluorinated Graphene/CoAl-Layered Double Hydroxide Composites as Electrode Materials for Supercapacitors. *ACS Appl. Mater. Interfaces* 9, 5204 (2017).

43. L. Shao, J. Hong, S. Wang, F. Wu, F. Yang, X. Shi, and Z. Sun, Urchin-Like FeS_2 Hierarchitectures Wrapped with N-Doped Multi-wall Carbon Nanotubes@rGO as High-Rate Anode for Sodium Ion Batteries. *J. Power Sources* 491, 229627 (2021).